

A passive eddy current damper for vibration suppression of a force sensor

Weihai Chen¹, Jun Jiang¹, Jingmeng Liu¹, Shaoping Bai² and Wenjie Chen³

¹ School of Automation Science and Electrical Engineering, Beihang University, Beijing, People's Republic of China

² Department of Mechanical and Manufacturing Engineering, Aalborg University, Aalborg, Denmark

³ Mechatronics group, Singapore Institute of Manufacturing Technology, Singapore

E-mail: junjiang@asee.buaa.edu.cn

Received 29 October 2012, in final form 12 December 2012

Published 23 January 2013

Online at stacks.iop.org/JPhysD/46/075001

Abstract

High performance force sensors often encounter the problem of vibrations during the process of calibration and measurement. To address this problem, this paper presents a novel passive eddy current damper (ECD) for vibration suppression. The conceived ECD utilizes eight tubular permanent magnets, arranged in Halbach array, and a conductive copper rod to generate damping. The ECD does not require an external power supply or any other electronic devices. In this paper, an accurate, analytical model for calculating the magnetic field distribution and damping coefficient is developed. The dynamics of the system is obtained by applying an energy method and an equivalent pseudo-rigid-body model. Moreover, finite element simulations are conducted to optimize the design. Experiments are carried out to validate the effectiveness of the design. The results indicate that the proposed ECD has a damping coefficient of 4.3 N s m^{-1} , which can provide a sufficient damping force to quickly suppress the sensor's vibration within 0.1 s.

(Some figures may appear in colour only in the online journal)

1. Introduction

The sensing part in a force sensor is usually composed of compliant structures, which are extremely sensitive to external disturbances, such that the vibration of the sensitive part usually makes the calibration process rather difficult and time consuming. Moreover, when the force sensor is exposed to a harsh environment, excessive vibrations may be detrimental to the structural integrity of structures or may adversely affect the performance of the sensor. Therefore, it is necessary to integrate a damper in a force sensor to suppress vibrations. Various approaches have been employed to isolate vibrations [1]. A commonly used method is to incorporate a tuned-mass damper (TMD) into the system that needs to be damped [2]. The TMD chooses appropriate mass and stiffness to make the natural frequency match the resonant mode of the structure. Another approach is to utilize viscoelastic

materials such as rubbers, polymers and some adhesives [3]. Shearing of viscoelastic materials dissipates vibrational energy as heat that is generated when the material is stressed by deformation. Additionally, some smart materials, such as magnetorheological fluids (MR) and electrorheological fluids (ER), have also been used to suppress vibrations [4, 5]. These materials can change from a liquid to a semi-solid state when exposed to a magnetic or electric field.

However, each of the aforementioned approaches has its limitations when applied to force sensors: they are either temperature sensitive or too bulky to be integrated into a force sensor. Over the past two decades, an alternative method for vibration suppression, the ECD, was proposed. According to electromagnetic field theory, eddy currents are induced either by the movement of the conductor in the static field or by changing the strength of the magnetic field. In the case of a force sensor, the vibration of the sensitive part causes a

relative motion between the magnet and the conductor, thus eddy currents are induced. The induced eddy currents then create a repulsive force that is proportional to the velocity of the conductor. The eddy current generation causes the vibration of the force sensor to dissipate through the Joule heating generated in the conductor part.

Applications of eddy currents for damping purposes have been widely investigated for several decades. Examples of these efforts can be seen in magnetic braking systems [6, 7], lateral vibration control of rotating machinery [8], vibration suppression of mechanical structures [9–11] and vibration isolation in suspension [12] and levitation systems [13–15]. More specifically, Sodano *et al* [9] proposed a passive ECD to suppress a beam's vibration. In his study, a detailed mathematical model for both the damping system and its interaction with the beam was developed. Subsequently, by replacing the permanent magnet (PM) with an electromagnet, Sodano and Inman [10] introduced an active ECD for vibration control of a cantilever beam. In addition, Ebrahimi *et al* [12] developed a new ECD for vehicle suspension using alternately arranged tubular permanent magnets (PMs) and iron poles, the scaled-down prototype fabricated could reach a damping coefficient as high as 53 N s m^{-1} . Teshima *et al* [13] investigated the effect of ECDs on the vibrational properties in superconducting levitations. Elbuken *et al* [15] proposed an eddy current damping mechanism to suppress vibrations and ensure stability by placing a conductive plate underneath the levitated object. Lin *et al* [16] designed an eddy current damping system to suppress the vibration of a flexure-based positioning stage. In addition to the applications of eddy currents, Zuo *et al* [17] introduced a new type of electromagnetic damper with increased energy density. They split the magnetic field into multiple ones with alternating directions so as to reduce the electrical resistance of the eddy current loops and increase the damping coefficient. Graves *et al* [18] presented a theoretical comparison between electromagnetic dampers based on a motional emf and transformer emf. Tonoli [19] studied the dynamic characteristics of ECDs. More applications and developments on ECDs can be seen in the review by Sodano and Bae [20]. Although ECDs have been widely used in many fields for its compactness, high reliability and non-contact characteristics, the application of eddy currents in vibration suppression of a force sensor has not been addressed in the literature. Therefore, the motivation of this study is to introduce a novel passive ECD to suppress the vibration of the sensitive part in a force sensor.

The rest of this paper is organized as follows: in section 2, the conceptual design of the force sensor and integrated ECD are described. A detailed mathematical model is developed in section 3 to estimate the magnetic field distribution and damping coefficient. In section 4 the dynamics of the force sensor and its interaction with the ECD is obtained through an energy method and a pseudo-rigid-body model (PRBM). Simulations from finite element software COMSOL Multiphysics are included in section 5 and compared with experimental results in section 6. The work is discussed in section 7 and concluded in section 8.

2. Mechanical structure description

2.1. Sensor system

Figure 1(a) shows a 3D model of the developed force sensing system. It consists of four main parts:

- A compound compliant mechanism serving as the sensor body.
- A grating-based displacement measurement unit including an optical read head and a glass grating scale.
- A bracket for mounting the read head and providing a gap between the read head and the grating scale.
- A probe which is attached to the centre of the sensor body acting as an interface to external forces.

Unlike conventional strain-gauge-based force sensing systems, the developed force sensor measures a force through measuring the displacement of the movable member suspended by a compliant mechanism. When a force is applied to the probe, the grating scale, which is firmly attached to the surface of the movable plate, has a relative movement against the read head, thus a pulse signal generates. The displacement of the movable member is measured through counting the peak numbers of the signal. An advantage of using grating scanning technique is that the displacement signal is digital which can immunize outside electromagnetic noises, so that the obtained displacement is precise and stable.

Our force sensor is specially designed to have a large measurement range and two-stage force resolutions. The working principle of the sensor body (compliant mechanism) is demonstrated as shown in figure 1(b), together with the top view in figure 1(c). The movable plate in the compliant mechanism is suspended by four compliant Roberts mechanisms (flexure joint B) [21] that are linked to the intermediate block in a symmetrical layout. The intermediate block is then supported by four flexural beams (flexure joint A) that are also arranged in symmetry. This arrangement can ensure the movable plate minimize the parasitic motion in other directions and possess a smooth linear translational movement under application of a force. In addition, there are two hard-stoppers between the intermediate block and the base frame, so that the movable plate possesses two constant stiffness values within its workspace. The low stiffness is applicable for small range and fine resolution force measurement, while the high stiffness is for large range and coarse resolution force measurement.

2.2. Eddy current damper

Figure 2 shows a prototype of the proposed ECD integrated with the force sensor. The ECD mainly consists of a copper rod and eight tubular PMs. The copper rod is attached to the centre of the movable plate performing as a perfect conductor for the ECD. The PMs which are embedded in the base frame are arranged in Halbach array. This arrangement can be explained by two reasons: (a) the Halbach array is proven to have the highest damping coefficient compared with other configurations [22]; (b) the Halbach array possesses its own continuous and closed magnetic flux path so that it is not needed

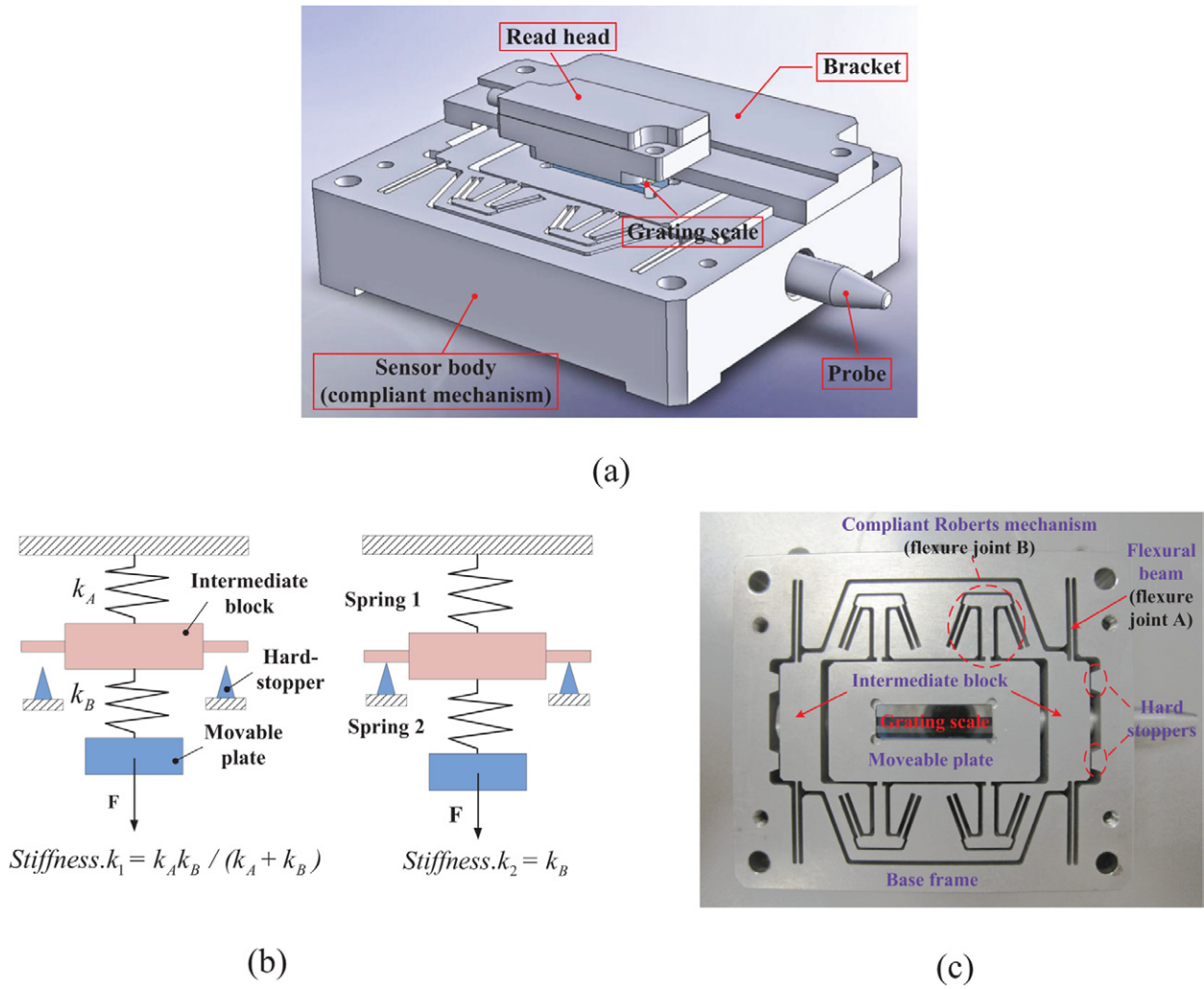


Figure 1. The flexure-based force sensor, (a) solid 3D model of the force sensing system, (b) schematic diagram of the sensor body (compliant mechanism), (c) top view of the sensor body.

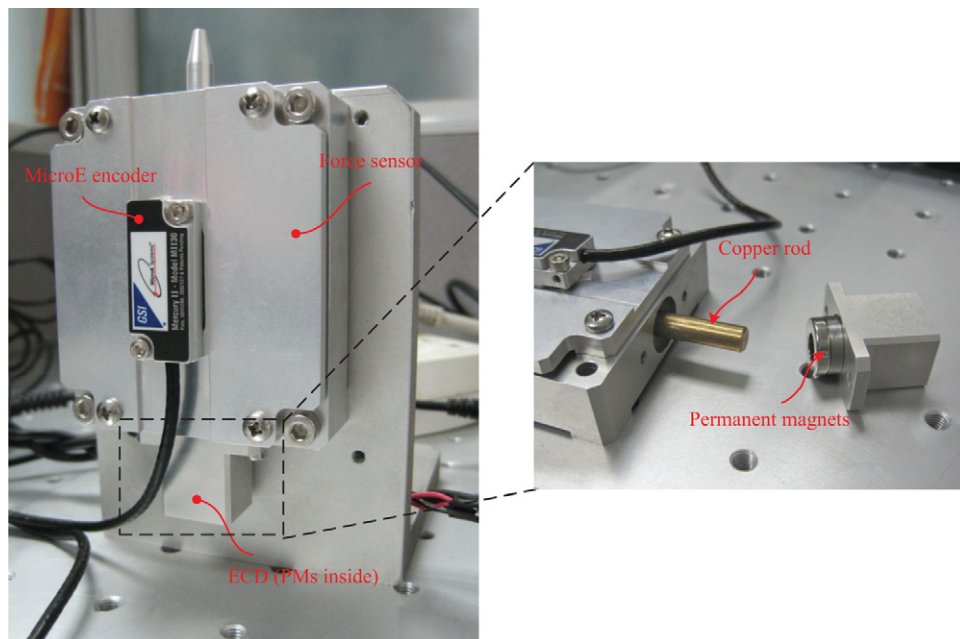


Figure 2. The innovative force sensor with a specially designed ECD.

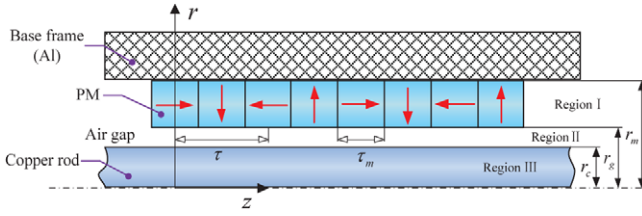


Figure 3. Configuration of the proposed ECD.

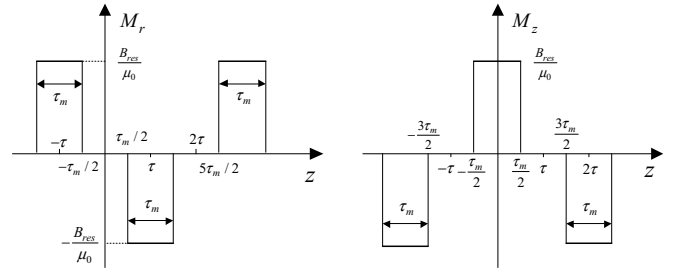


Figure 4. Distribution of M_r and M_z .

to laminate any steel strip on the base frame [23]. Therefore, the choice for the base frame material becomes flexible. In addition, there is an air gap between the copper rod and the inner rings of the PMs. Generally, the smaller the gap size, the larger the damping effectiveness of the ECD. In our case, the air gap thickness is set to 0.25 mm by considering the external size constraints and manufacturing restrictions.

During the process of measurement, when an external force is applied to or removed from the probe instantaneously, the movable plate oscillates near its equilibrium position, thus eddy currents are induced in the copper rod due to its relative motion with respect to the magnets, then the generated eddy currents produce a repulsive force that is proportional to the velocity of the copper rod such that the magnets and the moving conductor behave like a viscous damper. The eddy current generation causes the vibration of the force sensor to dissipate through the Joule heating generated in the conductor part.

To sum up, when the movable plate of the force sensor vibrates due to unexpected disturbances or instantaneous excitations, the eddy currents and a viscous damping force generate in the copper rod, making the vibration decay rapidly. One point that must be mentioned is that although the sensor body has two movable stages (the movable plate and the intermediate block), the proposed ECD is only used to suppress the vibration of the movable plate, because the stiffness of flexure joint B is much higher than that of flexure joint A. This assumption will be demonstrated in the following sections.

3. Magnetic field distribution and damping coefficient estimation

3.1. Magnetic field distribution

The simplified geometry model for the proposed ECD is illustrated in figure 3. In establishing analytical solutions for the magnetic field distribution in a Halbach magnetized tubular machine, the following assumptions are made:

- (i) The effect of the finite axial length is neglected, i.e. an infinite axial length of the ECD is considered, so that the field distribution is axially symmetric and periodic in the z direction.
- (ii) The relative differential permeability of the PM is supposed unity, $\mu_r = 1$.

Consequently, the magnetic field analysis can be confined to three regions along the r -direction, namely, the PM layer (region I) where the permeability is μ_0 , the air gap layer (region II) where the permeability is also μ_0 and the copper rod layer (region III) where the permeability and the conductivity

are $\mu_0\mu_1$ and σ , respectively. Assuming that any free current is absent in the interested regions, it is convenient to formulate the magnetic field distribution by means of scalar magnetic potential $\phi(r, z)$ defined by $\mathbf{H} = -\nabla\phi$, where \mathbf{H} is the magnetic field intensity. Therefore, the governing equations for the magnetic field distributions of the ECD can be described as follows [24–27]:

$$\nabla^2\phi^I = \nabla \cdot \mathbf{M} \quad \text{region I,} \quad (1a)$$

$$\nabla^2\phi^{II} = 0 \quad \text{region II,} \quad (1b)$$

$$\nabla^2\phi^{III} = 0 \quad \text{region III.} \quad (1c)$$

where \mathbf{M} is the magnetization. The superscripts denote the region numbers. Since the geometry of the ECD is axially symmetric, the scalar magnetic potential is the function of r and z only, thus equations (1a)–(1c) can be rewritten in the cylindrical coordinate system as

$$\frac{\partial}{\partial r} \left(\frac{1}{r} \frac{\partial}{\partial r} (r\phi^I) \right) + \frac{\partial^2\phi^I}{\partial z^2} = \nabla \cdot \mathbf{M} \quad \text{region I,} \quad (2a)$$

$$\frac{\partial}{\partial r} \left(\frac{1}{r} \frac{\partial}{\partial r} (r\phi^{II}) \right) + \frac{\partial^2\phi^{II}}{\partial z^2} = 0 \quad \text{region II,} \quad (2b)$$

$$\frac{\partial}{\partial r} \left(\frac{1}{r} \frac{\partial}{\partial r} (r\phi^{III}) \right) + \frac{\partial^2\phi^{III}}{\partial z^2} = 0 \quad \text{region III.} \quad (2c)$$

In addition, the orthogonal magnetization \mathbf{M} can be expressed as

$$\mathbf{M} = M_r \mathbf{e}_r + M_z \mathbf{e}_z,$$

where M_r and M_z denote the components of \mathbf{M} in the radial and axial directions, respectively. Figure 4 shows the distribution of M_r and M_z , which can be expanded into Fourier series of the forms

$$M_r(z) = \sum_{n=1}^{\infty} M_{rn} \sin(\omega_n z), \quad (3a)$$

$$M_z(z) = \sum_{n=1}^{\infty} M_{zn} \cos(\omega_n z), \quad (3b)$$

where

$$\omega_n = \frac{(2n-1)\pi}{\tau},$$

$$M_{rn} = -\frac{4B_{\text{res}}}{\mu_0\tau\omega_n} \sin\left(\frac{\omega_n\tau}{2}\right) \sin\left(\frac{\omega_n\tau_m}{2}\right),$$

$$M_{zn} = \frac{4B_{\text{res}}}{\mu_0\tau\omega_n} \sin\left(\frac{\omega_n\tau_m}{2}\right),$$

here B_{res} is the residual magnetic flux density, τ is the pole pitch of the ECD, and τ_m is the thickness of a single piece

of PMs. Therefore, the solutions of Poissons equation and Laplaces equation in equations (1a)–(1c) can be obtained as

$$\phi^I(r, z) = \sum_{n=1}^{\infty} \left[a_n^I I_0(\omega_n r) + b_n^I K_0(\omega_n r) - \frac{2c_1 M_{rn}}{\omega_n^2} \right] \cdot [c_n^I \cos(\omega_n z) + d_n^I \sin(\omega_n z)], \quad (4a)$$

$$\phi^{II}(r, z) = \sum_{n=1}^{\infty} [a_n^{II} I_0(\omega_n r) + b_n^{II} K_0(\omega_n r)] \cdot [c_n^{II} \cos(\omega_n z) + d_n^{II} \sin(\omega_n z)], \quad (4b)$$

$$\phi^{III}(r, z) = \sum_{n=1}^{\infty} [a_n^{III} I_0(\omega_n r) + b_n^{III} K_0(\omega_n r)] \cdot [c_n^{III} \cos(\omega_n z) + d_n^{III} \sin(\omega_n z)], \quad (4c)$$

where I_0 and K_0 are the modified Bessel functions of the first and the second kinds of zero order, respectively. The coefficient c_1 is defined as [28, 29]

$$c_1 = \frac{1}{r_g + r_m},$$

where r_g and r_m are the inner and outer radii of the PMs, respectively. The parameters a_n^q , b_n^q , c_n^q and d_n^q ($q = I, II, III$) are determined by the boundary conditions:

$$H_z^I(r_m, z) = M_z(z), \quad (5a)$$

$$H_z^I(r_g, z) = H_z^{II}(r_g, z), \quad (5b)$$

$$B_r^I(r_g, z) = B_r^{II}(r_g, z), \quad (5c)$$

$$H_z^{II}(r_c, z) = H_z^{III}(r_c, z), \quad (5d)$$

$$B_r^{II}(r_c, z) = B_r^{III}(r_c, z), \quad (5e)$$

$$\phi^{III}(0, z) = 0, \quad (5f)$$

where H_z^q and B_r^q are the axial components of magnetic field intensity and radial components of magnetic flux density at region q , respectively. Therefore, the field solutions that satisfy the boundary conditions can be obtained as

$$H_z^I(r, z) = \sum_{n=1}^{\infty} \omega_n \left[A_n^I I_0(\omega_n r) + B_n^I K_0(\omega_n r) - \frac{2c_1 M_{rn}}{\omega_n^2} \right] \cdot \cos(\omega_n z), \quad (6a)$$

$$H_z^{II}(r, z) = \sum_{n=1}^{\infty} \omega_n [A_n^{II} I_0(\omega_n r) + B_n^{II} K_0(\omega_n r)] \cdot \cos(\omega_n z), \quad (6b)$$

$$H_z^{III}(r, z) = \sum_{n=1}^{\infty} \omega_n [A_n^{III} I_0(\omega_n r)] \cdot \cos(\omega_n z), \quad (6c)$$

$$B_r^I(r, z) = \mu_0 \cdot \sum_{n=1}^{\infty} \omega_n \left[A_n^I I_1(\omega_n r) - B_n^I K_1(\omega_n r) - \left(c_1 r + \frac{c_2}{r} \right) \frac{M_{rn}}{\omega_n} \right] \cdot \sin(\omega_n z) \quad (6d)$$

$$B_r^{II}(r, z) = \mu_0 \cdot \sum_{n=1}^{\infty} \omega_n [A_n^{II} I_1(\omega_n r) - B_n^{II} K_1(\omega_n r)] \cdot \sin(\omega_n z), \quad (6e)$$

$$B_r^{III}(r, z) = \mu_0 \cdot \sum_{n=1}^{\infty} \omega_n [A_n^{III} I_1(\omega_n r)] \cdot \sin(\omega_n z), \quad (6f)$$

where I_1 and K_1 are the modified Bessel functions of the first and second kinds of order one, respectively. The coefficients A_n^I, B_n^I, A_n^{II} and B_n^{II} are defined in appendix A for further details. Moreover, the coefficient c_2 is defined as

$$c_2 = \frac{r_g r_m}{r_g + r_m}.$$

3.2. Damping coefficient estimation

The eddy current phenomenon occurs either in a conductor in a time-varying magnetic field, or in a conductor that moves in a constant magnetic field. The former contribution is associated with the transformer eddy current, whereas the latter is associated with the motional eddy current [12]. The total induced emf is given by

$$E = E_{\text{trans}} + E_{\text{motional}} = - \int_s \frac{\partial \mathbf{B}}{\partial t} \cdot d\mathbf{s} + \int_c (\mathbf{v} \times \mathbf{B}) \cdot d\mathbf{l}, \quad (7)$$

where \mathbf{v} and \mathbf{B} are the velocity of the conductor related to the magnetic flux, and the magnetic flux density, respectively. Since the magnetic flux density is constant in this case, the first term of the right-hand side of equation (7) vanishes. Due to absent of free currents, the current density \mathbf{J} induced in the conductive copper rod moving in the z direction is expressed by computing

$$\mathbf{J} = \sigma(\mathbf{v} \times \mathbf{B}). \quad (8)$$

According to the Lorentz law, the damping force due to the eddy current is defined by

$$\mathbf{F} = \int_V \mathbf{J} \times \mathbf{B} dV, \quad (9)$$

where V is the volume of the conductor. Since the velocity of the copper rod is in the z direction, the axial component of the magnetic flux density B_z does not contribute to the generation of damping force. So the damping force in the z direction can be simplified as [9]

$$\begin{aligned} F &= -e_z \frac{n}{2} \sigma \tau_m v_z \int_0^{2\pi} \int_0^{r_c} r B_r^2(r, z_0) dr d\theta \\ &= -e_z \pi n \sigma \tau_m v_z \int_0^{r_c} r B_r^2(r, z_0) dr, \end{aligned} \quad (10)$$

where n is the number of the PMs used in the ECD and B_r is the radial component of the magnetic flux density in region III, which is calculated from equation (6c), $B_r = B_r^{III}$. So the equivalent constant damping coefficient, C , for the proposed ECD is obtained by

$$C = \pi n \sigma \tau_m \int_0^{r_c} r B_r^2 dr. \quad (11)$$

Equations (10) and (11) are employed to compute the damping force and damping coefficient for the proposed ECD configuration, respectively.

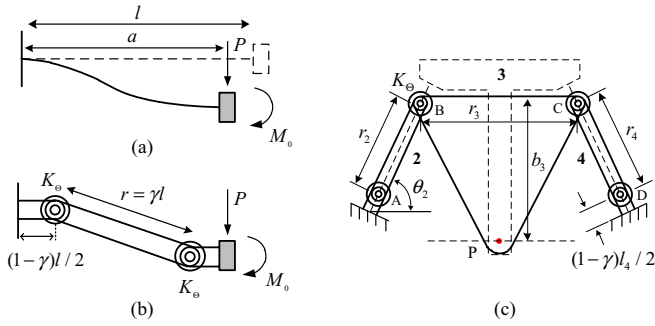


Figure 5. (a) Flexible fixed-guided beam and (b) pseudo-rigid-body model of a single beam and (c) pseudo-rigid-body model of a compliant Roberts mechanism.

4. Dynamic modelling

As discussed in section 2, the sensor body (compliant mechanism) consists of two movable stages, each movable stage being suspended by a group of flexure joints. Therefore, it can be considered as a 2-DOF dynamic system as described presently.

4.1. Stiffness analysis

In the 2-DOF system, there are two groups of flexure joints, namely, flexure joint A and B, being used. The first group of flexure joints (flexure joint A) which supports the intermediate block is composed of four flexural beams. Therefore, the overall stiffness for the first group can be simply estimated using linear beam theory as

$$k_A = 4Ew_a \left(\frac{t_a}{l_a} \right)^3, \quad (12)$$

where E is Young's modulus, l_a , w_a and t_a are the length, width and thickness of the flexural beam, respectively.

The second group of flexure joints (flexure joint B) that supports the movable plate is composed of four compliant Roberts mechanisms. The overall stiffness is derived from a PRBM of a single Roberts mechanism [30, 31]. In the PRBM, two flexural beams are replaced by four identical torsional springs and two rigid links, as depicted in figure 5. The stiffness for this group of flexure joints can be obtained through

$$k_B \approx \frac{F}{\Delta x}, \quad (13)$$

where Δx and F are the displacement of the movable plate and the force required to displace the movable plate, respectively. The two parameters are given by

$$\begin{aligned} \Delta x &= r_2(\cos \theta_2 - \cos \theta_{20}) + \frac{r_3}{2}(\cos \theta_3 - 1) + b_3 \sin \theta_3, \\ F &= 4K_\Theta \left[(2 - h_{32})\Delta\theta_2 + (2h_{42} - h_{32})\Delta\theta_4 \right. \\ &\quad \left. - (1 + h_{42} - 2h_{32})\Delta\theta_3 \right] \\ &\quad \times \left[r_2 \sin \theta_2 + h_{32} \left(\frac{r_3}{2} \sin \theta_3 - b_3 \cos \theta_3 \right) \right]^{-1}, \end{aligned}$$

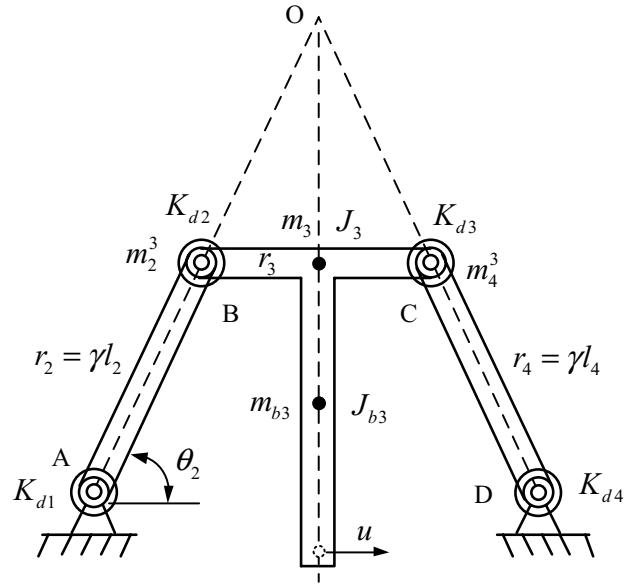


Figure 6. Pseudo-rigid-body dynamic model of a single Roberts mechanism.

where b_3 is the perpendicular distance from the centre of link 3 to the coupler point (see in figure 5). r_i , θ_i and θ_{i0} are the PRB length, final angle and initial angle of link i , respectively. h_{32} and h_{42} are kinematic coefficients, and K_Θ is the spring constant (see [30] for details). Apparently, the stiffness of flexure joint B is configuration dependent. A mean value over a small range of joint deflection can be used as the overall stiffness of the joint.

4.2. Equivalent mass analysis

In order to model the equivalent mass of the flexure joints, energy methods are used to relate the kinetic energy of the flexure joints to that of an equivalent pseudo-rigid-body dynamic model (PRBDM) system. Generally, one lumped mass and two torsional springs are needed for the dynamic equivalence of one flexible link, so the equivalent lumped mass for flexure joint A can be calculated by [32]

$$m_{eA} = \frac{1}{4}m_a + \frac{J_a}{r_a^2}, \quad (14)$$

where m_a and J_a are the mass and mass moment of inertia of flexure joint A, respectively, r_a is the PRB length of the flexural beam, which is defined by $r_a = \gamma l_a$.

Considering an individual compliant Roberts mechanism, four torsional springs and two lumped masses are added in the PRBDM, as shown in figure 6.

Therefore, the kinetic energy for the PRBDM system can be expressed as follows:

$$\begin{aligned} T &= \frac{1}{2}m_{eB}u^2 = \frac{1}{2}m_2^3v_B^2 + \frac{1}{2}m_4^3v_C^2 + \left(\frac{1}{2}m_3v_{m3}^2 + \frac{1}{2}J_3\omega_3^2 \right) \\ &\quad + \left(\frac{1}{2}m_{b3}v_{b3}^2 + \frac{1}{2}J_{b3}\omega_3^2 \right), \end{aligned} \quad (15)$$

where m_{eB} is the equivalent mass of a single compliant Roberts mechanism. m_i and J_i are the mass and mass moment of inertia of link i , ($i = 3, b3$), respectively. m_2^3 and m_4^3 are the

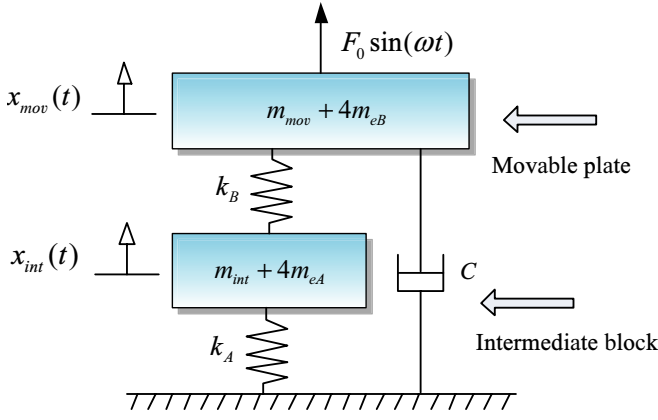


Figure 7. Schematic diagram of the vibration isolation system.

lumped masses of the two flexible links, and are given in [32]. Moreover, u is the velocity of the coupler point, ω_3 is the angular velocity of link 3, v_B , v_C , v_{m3} and v_{b3} are the velocities of corresponding points, respectively. It is well known from the kinematic analysis of the rigid-body motion of a four-bar linkage that

$$\begin{aligned} v_B = v_C = f(\theta_2, u), \quad v_{m3} = g(\theta_2, u), \\ v_{b3} = h(\theta_2, u), \quad \omega_3 = q(\theta_2, u). \end{aligned} \quad (16)$$

Therefore, the equivalent mass of a single compliant Roberts mechanism can be derived as

$$m_{eB} = \alpha(m_2^3 + m_4^3) + \beta m_3 + \psi m_{b3} + \frac{1}{\chi^2}(J_3 + J_{b3}), \quad (17)$$

where the coefficients α , β , ψ and χ are defined in appendix B.

4.3. Dynamic equations

Figure 7 shows the simplified dynamic model of the entire sensor body. Assuming that the internal damping of the system can be neglected, the differential equations governing the motion of the system are presented as follows:

$$\begin{aligned} \begin{bmatrix} F_0 \\ 0 \end{bmatrix} \sin \omega t = \begin{bmatrix} m_{\text{mov}} + 4m_{eB} & 0 \\ 0 & m_{\text{int}} + 4m_{eA} \end{bmatrix} \begin{bmatrix} \ddot{x}_{\text{mov}}(t) \\ \ddot{x}_{\text{int}}(t) \end{bmatrix} \\ + \begin{bmatrix} C & 0 \\ 0 & 0 \end{bmatrix} \begin{bmatrix} \dot{x}_{\text{mov}}(t) \\ \dot{x}_{\text{int}}(t) \end{bmatrix} + \begin{bmatrix} k_B & -k_B \\ -k_B & k_A + k_B \end{bmatrix} \begin{bmatrix} x_{\text{mov}}(t) \\ x_{\text{int}}(t) \end{bmatrix}. \end{aligned} \quad (18)$$

To solve the motion equations, let $F_0 \sin \omega t$ be expressed in exponential form as $F_0 e^{j\omega t}$ and assume that the steady-state solution can be written as

$$\mathbf{X}(t) = \mathbf{X} e^{j\omega t} = \begin{bmatrix} X_{\text{mov}} \\ X_{\text{int}} \end{bmatrix} e^{j\omega t}, \quad (19)$$

where X_{mov} and X_{int} are the vibration amplitudes of the movable plate and the intermediate block, respectively.

Substituting equation (19) into (18) yields

$$\begin{aligned} \begin{bmatrix} X_{\text{mov}} \\ X_{\text{int}} \end{bmatrix} = \frac{1}{\det(-\omega^2 \tilde{\mathbf{M}} + j\omega \mathbf{C} + \mathbf{K})} \\ \times \begin{bmatrix} \kappa - \omega^2 \zeta & k_B \\ k_B & k_B - \omega^2 \eta + j\omega C \end{bmatrix} \begin{bmatrix} F_0 \\ 0 \end{bmatrix}, \end{aligned} \quad (20)$$

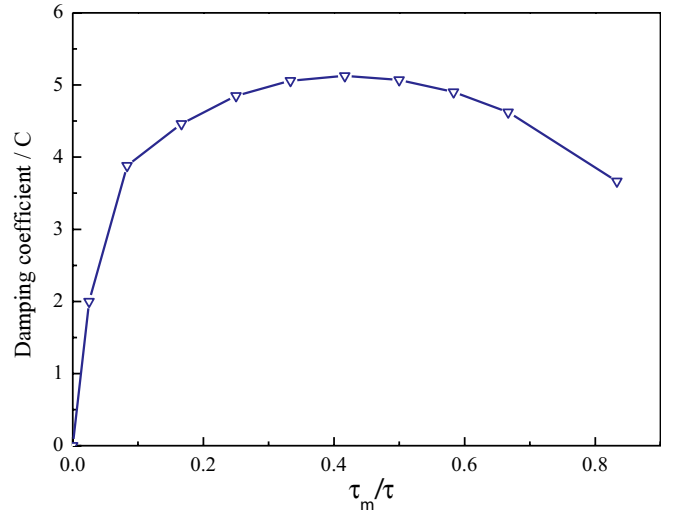


Figure 8. Damping coefficient versus normalized magnetic thickness.

Table 1. Parameters of the conductor and magnets.

Property (symbol)	Value
Number of PMs (n)	8 mm
Radius of copper rod (r_c)	3 mm
Inner radius of PMs (r_g)	3.25 mm
Outer radius of PMs (r_m)	6.5 mm
Pole pitch (τ)	6 mm
Magnet thickness (τ_m)	3 mm
Residual flux density of PMs (B_{res})	1.21 T
Permeability in vacuum (μ_0)	$4\pi \times 10^{-7} \text{ H m}^{-1}$
Relative permeability of copper rod (μ_1)	1.33
Conductivity of copper rod (σ)	$5.9 \times 10^{-7} \Omega^{-1} \text{ m}^{-1}$

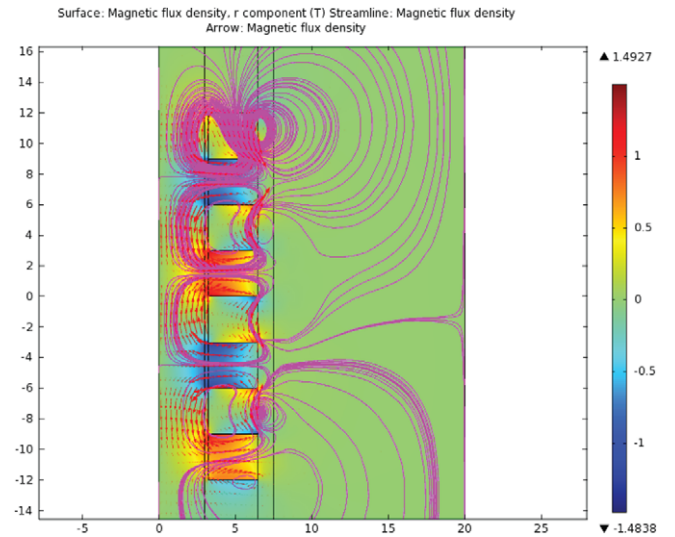


Figure 9. 2D axisymmetric FE simulation of the ECD.

where $\tilde{\mathbf{M}}$, \mathbf{C} , and \mathbf{K} are the system mass matrix, damping matrix and stiffness matrix respectively (defined in equation (18)). The parameters κ , ζ , and η are defined as follows:

$$\kappa = k_A + k_B, \quad \zeta = m_{\text{int}} + 4m_{eA}, \quad \eta = m_{\text{mov}} + 4m_{eB}.$$

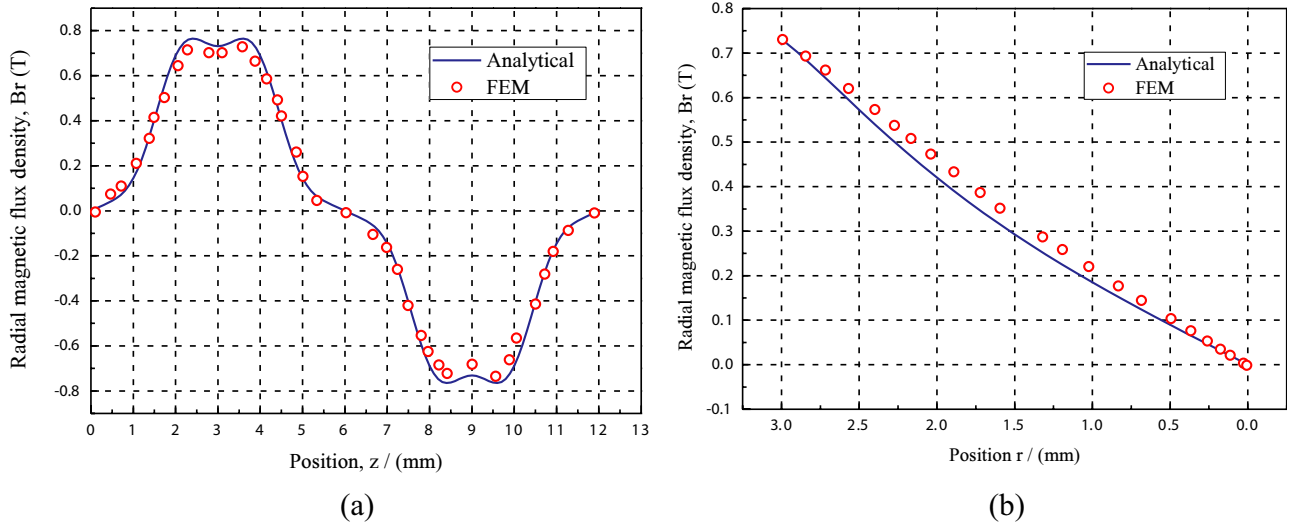


Figure 10. Comparison of radial flux density component (a) variation of B_r as a function of z , at $r = 3$ mm and (b) variation of B_r as a function of r , at $z = 3$ mm.

Therefore, the vibration amplitude of the movable plate in frequency domain is

$$\frac{X_{\text{mov}}}{F_0} = \frac{\kappa - \omega^2 \zeta}{\sqrt{[(\kappa - \omega^2 \zeta)(k_B - \omega^2 \eta) - k_B^2]^2 + \omega^2 C^2 (\kappa - \omega^2 \zeta)^2}} \quad (21)$$

Substituting equation (11)–(14) and (17) into equation (21), the dynamics of the force sensor and its interaction with the proposed ECD is determined.

5. Numerical analysis of the ECD

Figure 8 reflects the variation of the damping coefficient in terms of the normalized magnetic thickness. It is observed that the maximum damping coefficient is obtained at τ_m/τ equal to 0.45. Consequently, the optimal value for the normalized magnetic thickness is chosen as 0.5 for the convenience of fabrication. The other geometric parameters are selected by considering the external size constraints, and are summarized in table 1. The material of the magnets is NdFeB alloy.

Simulations were conducted for a two-dimensional axisymmetric model of the damper, using the ac/dc module in software Comsol Multiphysics. In this simulation, the physical model was meshed with 3-nodes, linear, triangular elements. The PMs were magnetized in accordance with figure 3. The stationary slover was employed to solve the magnetic field within a finite boundary. Figure 9 displays the flux density contour obtained by FE simulation for the conceived prototype. It is observed that the magnetic flux distribution at the base frame is relatively weak, while the radial flux density at the copper rod is concentrated and enhanced, causing more eddy current induction such that the damper is more effective. Figure 10 compares the numerically and analytically calculated distributions of the radial flux density component, B_r , as functions of the axial position z at a constant

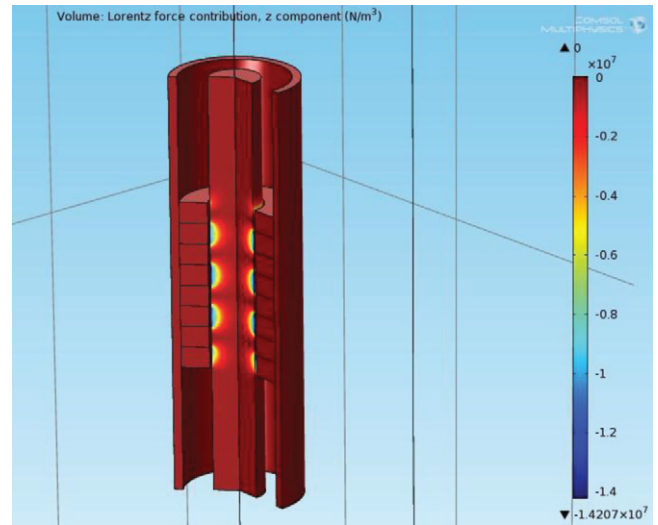


Figure 11. Contour of Lorentz force distribution.

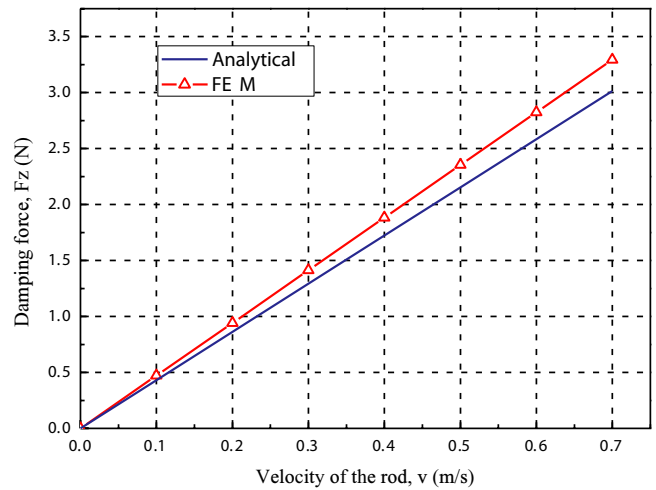


Figure 12. Analytically and numerically calculated force-velocity relationship.

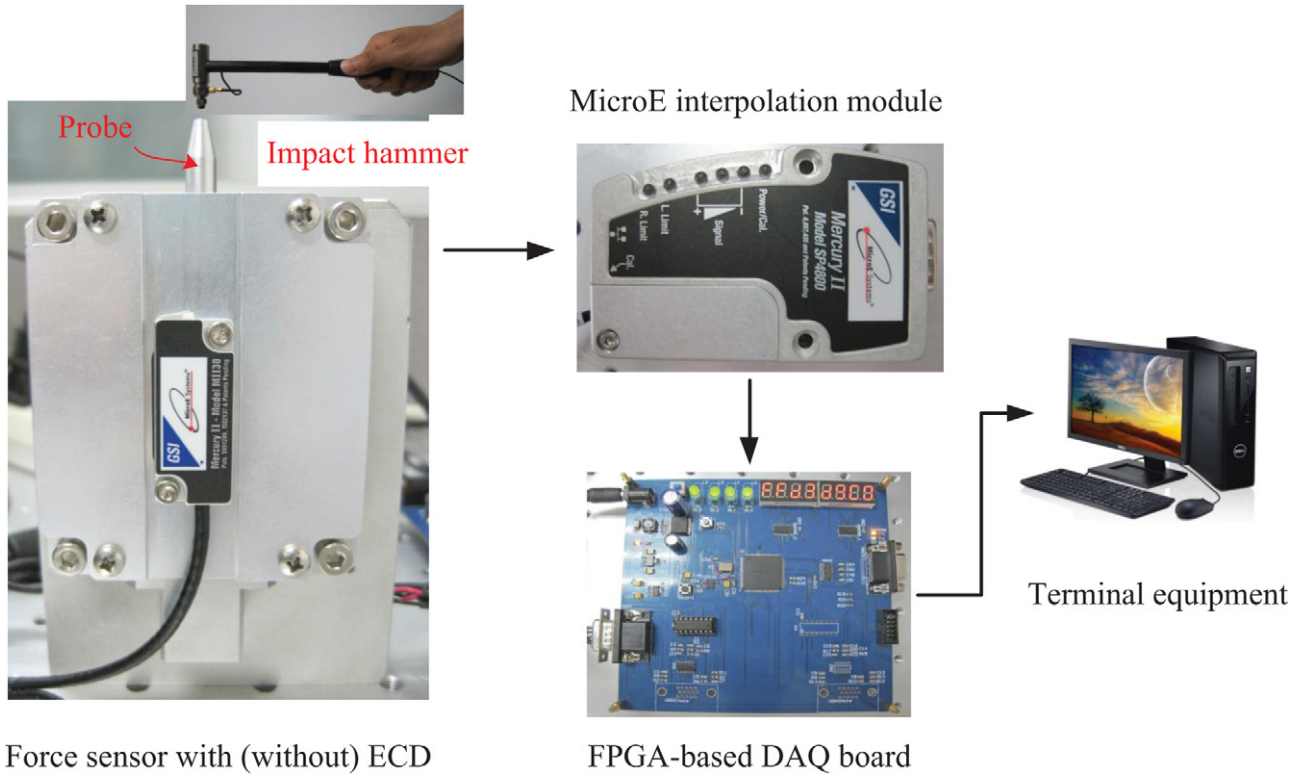


Figure 13. Schematic diagram of dynamic test.

radius, $r = 3$ mm (figure 10(a)), and the radial position r at $z = 3$ mm (figure 10(b)), respectively. It can be seen that the analytical solutions agree extremely well with the finite element predictions, and the flux density at region III is periodic with respect to the axial position.

In another simulation, the damping force was estimated. According to equation (10), the damping force is calculated by integrating the Lorentz force distribution generated in the copper rod, as illustrated in figure 11. Since the damping force varies with the velocity of the copper rod, it was calculated in COMSOL across a range of excitation speeds. The force-velocity relationship is plotted in figure 12. It can be seen that the theoretical prediction is very close to the FE result, and the damping coefficient can be obtained from the slope of force-velocity curve due to the linear relationship.

6. Experiment results

Experiments have been carried out on a prototype of the new damper. The schematic diagram of the test rig is shown in figure 13. The sensor body was fabricated through wire electric discharge machining (EDM). The geometric parameters of the two flexure joints are summarized in table 2. For the experiment, the resolution of the measurement unit and the maximal output frequency of the signals were set to 50 nm and 10 MHz, respectively. The impact excitation was input by an impact hammer. The MicroE II 4800 linear encoder was used to measure the vibration under the impact excitation. The signals obtained from the encoder were transmitted to an FPGA-based data acquisition board for signal conditioning

Table 2. Physical properties of the flexure joints (A and B).

Property (symbol)	Value
Length of flexure joint A (l_a)	14.5 mm
Length of flexure joint A (w_a)	15.0 mm
Thickness of flexure joint A (t_a)	0.32 mm
Length of flexible links in joint B (l_2, l_4)	8.20 mm
Width of flexible links in joint B (w_2, w_4)	15.0 mm
Thickness of flexible links in joint B (t_2, t_4)	0.40 mm
Length of rigid link 3 in joint B (l_3)	7.35 mm
Length of coupler extension in joint B (b_3)	10.0 mm
Initial angle of link 2 in joint B (θ_{20})	70°
Initial angle of link 3 in joint B (θ_{30})	0
PRBM parameter (γ)	0.85
Material of sensor body	AL-7075
Youngs modulus of sensor body (E)	72 GPa
Density of sensor body (ρ)	$2.75 \times 10^3 \text{ kg m}^{-3}$

through a VGA port. The converted signals were then fed into the terminal equipment for Fourier analysis.

Figure 14 shows the impulse response of the force sensor. The decay time is significantly shortened from 9 to 0.1 s due to the contribution of the ECD. Figure 15 shows the frequency response of the force sensor. It can be concluded that the first mode of vibration is greatly suppressed by approximately 30 dB. Using the measured damping ratio and frequency response experiments we are able to determine the damping coefficient of the developed ECD.

Although the force sensor is a 2-DOF dynamic system, the resonance frequency of the second mode is around 1200 Hz (obtained from FE simulation), which is much higher than that of the first mode, and this has verified the assumption made in section 2.

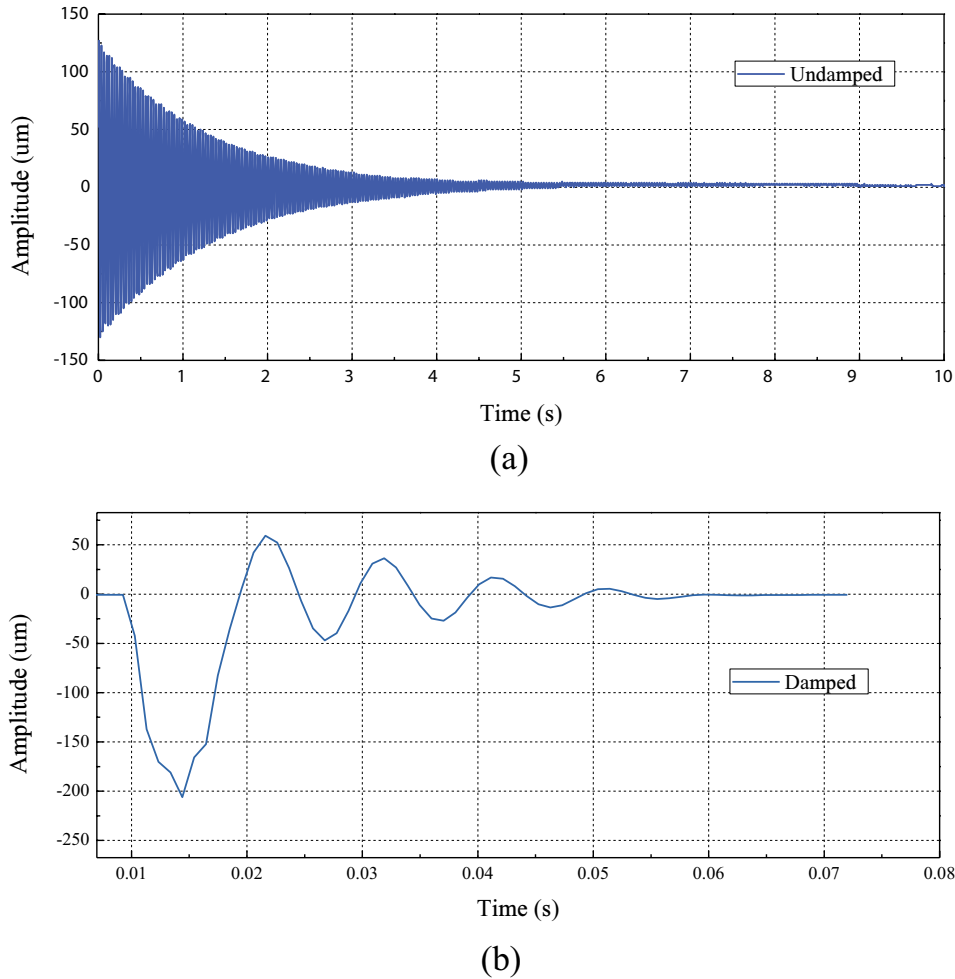


Figure 14. Experimentally measured impulse response of the force sensor, (a) without ECD and (b) with ECD.

7. Discussion

This paper has demonstrated the design, analysis and experiments of a novel passive ECD which attempts to suppress the vibration of a force sensor. Unlike conventional damping techniques, where the damper is mechanically coupled to the sensing body, the new method works under a non-contact mode, thus the damper has less influence on the sensing function, but contributes significantly to the reduction of undesired vibrations. Additionally, the newly developed damper is modular and easy to install. In terms of damping, the ECD can provide a large damping force with compact structures.

With the application of the ECD, the force sensor is not suitable for dynamic measurement of high frequency anymore. However, in our case and in most situations, the force sensors are intended for static or low-frequency tests. Therefore, the force sensors will have better performance with the integrated ECD. Although the cost of the ECD is not very appealing, compared with commercial passive dampers, the performance of the newly developed ECD in force sensor applications is still attractive. Our primary goal is to shorten the sensor’s calibration time due to vibrations. This tool will now enable us to characterize the force sensor more quickly and easily.

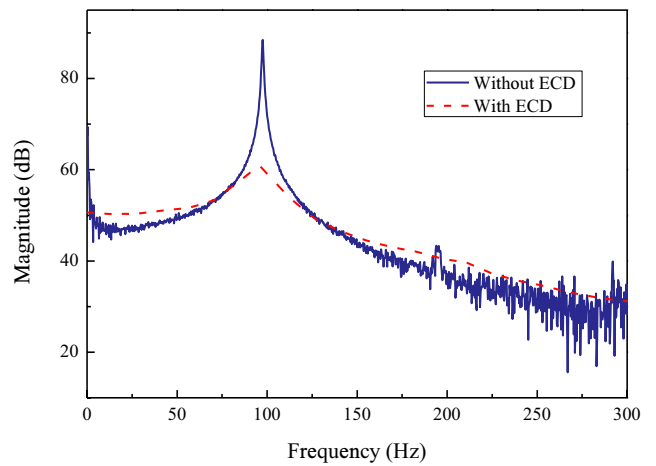


Figure 15. Frequency response with and without ECD.

8. Conclusion

In this paper, a newly developed force sensor with two-stage force resolutions (capable of measuring both micro-range and macro-range forces within one setup) and an ECD were introduced. This is the first time that an ECD has been successfully integrated into a force sensor to suppress the

vibration and protect the fragile components from damage. The structure of the ECD is innovative which makes the entire sensing system more compact and effective. A theoretical model for the generated damping force was derived by solving Poisson's equation and Laplace's equation with suitable boundary conditions. Furthermore, a systematic, analytical model for calculating the dynamics of a flexure-based 2-DOF system was developed. Both the simulation and experiment results were included to show the feasibility of the design. It has been found that the proposed eddy current damping mechanism could provide a large damping force to quickly suppresses the sensor's vibration.

Acknowledgments

This work is financially sponsored by the National Nature Science Foundation of China with Grants 91023036 and 51275018. This support is gratefully acknowledged. The authors would also like to express their appreciation to Beijing ZYHX Co. Ltd. for manufacturing some of the components for the experiment. In addition, we thank the reviewers for their comments to improve the quality of this work.

Appendix A

Define the following parameters:

$$N_1 = \frac{2c_1 M_{rn}}{\omega_n^2} + \frac{M_{zn}}{\omega_n}, \quad (A.1)$$

$$N_2 = \frac{2c_1 M_{rn}}{\omega_n^2}, \quad (A.2)$$

$$N_3 = \left(c_1 r_g + \frac{c_2}{r_g} \right) \frac{M_{rn}}{\omega_n}, \quad (A.3)$$

$A_n^I, B_n^I, A_n^{II}, B_n^{II}$ and A_n^{III} are the solutions of the following linear equations:

$$\begin{bmatrix} I_0(\omega_n r_m) & K_0(\omega_n r_m) & 0 & 0 & 0 \\ I_0(\omega_n r_g) & K_0(\omega_n r_g) & -I_0(\omega_n r_g) & -K_0(\omega_n r_g) & 0 \\ I_1(\omega_n r_g) & -K_1(\omega_n r_g) & -I_1(\omega_n r_g) & K_1(\omega_n r_g) & 0 \\ 0 & 0 & I_0(\omega_n r_c) & K_0(\omega_n r_c) & -I_0(\omega_n r_c) \\ 0 & 0 & I_1(\omega_n r_c) & -K_1(\omega_n r_c) & -\mu_1 I_1(\omega_n r_c) \end{bmatrix} \times \begin{bmatrix} A_n^I \\ B_n^I \\ A_n^{II} \\ B_n^{II} \\ A_n^{III} \end{bmatrix} = \begin{bmatrix} N_1 \\ N_2 \\ N_3 \\ 0 \\ 0 \end{bmatrix}.$$

Appendix B

The parameters are defined as follows:

$$\chi = \frac{r_3}{2} \text{tg}\theta_2 + b_3, \quad (B.1)$$

$$\alpha = \frac{r_3^2}{4\chi^2 \cos^2\theta_2}, \quad (B.2)$$

$$\beta = \left(1 - \frac{b_3}{\chi} \right)^2, \quad (B.3)$$

$$\psi = \left(1 - \frac{b_3}{2\chi} \right)^2. \quad (B.4)$$

References

- [1] http://www.cs.wright.edu/~jslater/SDTCOutreachWebsite/vibration_suppression_banner.pdf
- [2] Bae J S, Hwang J H, Roh J H, Kim J H, Yi M S and Lim J H 2012 *J. Sound Vib.* **331** 5669–84
- [3] Park S W 2001 *Int. J. Solids Struct.* **38** 8065–92
- [4] Spencer B F Jr, Dyke S J, Sain M K and Carlson J D 1997 *J. Eng. Mech.* **123** 230–8
- [5] Peel D J, Stanway R and Bullough W A 1996 *Smart Mater. Struct.* **5** 591–606
- [6] Heald M A 1988 *Am. J. Phys.* **56** 521–2
- [7] Cadwell L H 1996 *Am. J. Phys.* **64** 917–23
- [8] Genta G, Delpreta C, Tonoli A, Rava E and Mazzocchetti L 1992 *Proc. Int. Symp. on Magnetic Bearing (Washington, DC)* pp 255–64
- [9] Sodano H A, Bae J S, Inman D J and Belvin W K 2005 *J. Sound Vib.* **288** 1177–96
- [10] Sodano H A and Inman D J 2007 *J. Sound Vib.* **305** 596–613
- [11] Cheng T H and Oh I K 2009 *IEEE Trans. Magn.* **45** 2758–61
- [12] Ebrahimi B, Khamesee M B and Golnaraghi F 2009 *J. Phys. D: Appl. Phys.* **42** 075001
- [13] Teshima H, Tanaka M, Miyamoto K, Nohguchi K and Hinata K 1997 *Physica C* **274** 17–23
- [14] Elbuken C, Khamesee M B and Yavuz M 2006 *J. Phys. D: Appl. Phys.* **39** 3932–8
- [15] Elbuken C, Shameli E and Khamesee M B 2007 *IEEE Trans. Magn.* **43** 26–32
- [16] Lin C H, Hung S K, Chen M Y, Li S T and Fu L C 2008 *Int. Conf. on Control, Automation and Systems (COEX, Seoul)* pp 771–6
- [17] Zuo L, Chen X and Nayfeh S 2011 *J. Vib. Acoust.* **133** 041006
- [18] Graves K E, Toncich D and Iovenitti P G 2000 *J. Sound Vib.* **233** 441–53
- [19] Tonoli A 2007 *J. Sound Vib.* **301** 576–91
- [20] Sodano H A and Bae J S 2004 *Shock Vib. Digest* **36** 469–78
- [21] Hubbard N B, Wittwer J W, Kennedy A, Wilcox D L and Howell L L 2004 *Proc. ASME Int. Design Engineering Technical Conf. and Computers and Information in Engineering Conf. (Salt Lake City, UT)* pp 1–5
- [22] Ebrahimi B, Khamesee M and Golnaraghi F 2010 *Microsyst. Technol.* **20** 19–24
- [23] Tsai N C and Chiang C W 2010 *Mechatronics* **20** 596–603
- [24] Xia Z P, Zhu Z Q and Howe D 2004 *IEEE Trans. Magn.* **40** 1864–72
- [25] Wang J B, Jewell G W and Howe D 1999 *IEEE Trans. Magn.* **35** 1986–2000
- [26] Wang J B and Howe D 2005 *IEEE Trans. Magn.* **41** 2470–8
- [27] Edward E P 2001 *Permanent magnet and electromechanical devices, materials, analysis and applications* (San Diego, CA: Academic) p 162
- [28] Bianchi N 2000 *Proc. Conf. Rec. IEEE-IAS Annu. Meeting (Rome)* pp 21–8
- [29] Jang S M, Choi J Y, Lee S H, Cho H W and Jang W B 2004 *IEEE Trans. Magn.* **40** 2068–70
- [30] Roman G A and Wiens G J 2007 *Proc. ASME Int. Design Engineering Technical Conf. and Computers and Information in Engineering Conf. (Las Vegas, NV)* pp 127–35
- [31] Howell L L 2001 *Compliant Mechanisms* (New York: Wiley)
- [32] Yu Y Q, Howell L L, Lusk C, Yue Y and He M G 2005 *J. Mech. Des.* **127** 760